

## THE EFFECTS OF CLUMPS IN EXPLAINING X-RAY EMISSION LINES FROM HOT STARS

J. P. CASSINELLI

Department of Astronomy, University of Wisconsin—Madison, Madison, WI 53711; cassinelli@astro.wisc.edu

R. IGNACE

Department of Physics, Astronomy, and Geology, East Tennessee State University, Johnson City, TN 37614; ignace@etsu.edu

W. L. WALDRON

Eureka Scientific, Inc., 2452 Delmer Street, Oakland, CA 94602; wwaldron@satx.rr.com

J. CHO

Department of Astronomy and Space Science, Chungnam National University, Daejeon, Korea; jcho@cnu.ac.kr

AND

N. A. MURPHY AND A. LAZARIAN

Department of Astronomy, University of Wisconsin—Madison, Madison, WI 53711;

murphy@astro.wisc.edu, lazarian@astro.wisc.edu

Received 2007 December 20; accepted 2008 April 29

### ABSTRACT

It is now well established that stellar winds of hot stars are fragmentary and that the X-ray emission from stellar winds has a strong contribution from shocks in winds. *Chandra* high spectral resolution observations of line profiles of O and B stars have shown numerous properties that had not been expected. Here we suggest explanations by considering the X-rays as arising from bow shocks that occur where the stellar wind impacts on spherical clumps in the winds. We use an accurate and stable numerical hydrodynamic code to obtain steady state physical conditions for the temperature and density structure in a bow shock. We use these solutions plus analytic approximations to interpret some major X-ray features: the simple power-law distribution of the observed emission measure derived from many hot star X-ray spectra and the wide range of ionization stages that appear to be present in X-ray sources throughout the winds. Also associated with the adiabatic cooling of the gas around a clump is a significant transverse velocity for the hot plasma flow around the clumps, and this can help to understand anomalies associated with observed line widths, and the differences in widths seen in stars with high and low mass-loss rates. The differences between bow shocks and the planar shocks that are often used for hot stars are discussed. We introduce an “on the shock” approximation that is useful for interpreting the X-rays and the consequences of clumps in hot star winds and elsewhere in astronomy.

*Subject headings:* line: formation — shock waves — stars: early-type — stars: winds, outflows — X-rays: general — X-rays: stars

### 1. INTRODUCTION

Our goal is to explain with clump bow shocks many of the problems found in the survey of 17 normal OB stars by Waldron & Cassinelli (2007; hereafter WC07). Well-resolved spectral line profiles are found to be neither shifted nor skewed to the blue (i.e., shortward) as had been expected (e.g., MacFarlane et al. 1991). The line widths are broader for supergiants and stars with thick winds than for lower luminosity stars. It seems clear that X-rays are formed in numerous shock fragments distributed throughout the wind.

The topic of high nonradiative equilibrium temperatures in the winds of hot stars began with the discovery of superionization stages seen in the FUV spectra obtained with the *Copernicus* satellite. Lamers & Morton (1976) analyzed the spectrum of  $\zeta$  Pup (O4 If) and found strong lines of O VI (1040 Å) and N V (1240 Å). These ionization stages seemed to require that the winds are “warm,” with temperatures of about  $2 \times 10^5$  K. Alternatively, the ions could be produced by the Auger ionization process whereby two electrons are removed from the dominant ionization stage following K-shell ionization by X-rays (Cassinelli et al. 1978). Cassinelli & Olson (1979) used a “thin corona plus cool wind” model to show that the X-rays from a spatially thin corona

plus the Auger process could explain observed boundaries in the H-R diagram: a sharp cutoff in the presence of the O VI UV line that occurs at spectral type B0, a cutoff of the superionization line of N V at B1.5, and similar ones for C IV at B5 and Si IV at B8 (Cassinelli & Abbott 1981). In each case the high ions could be explained by the removal of two electrons from the *dominant* stage of ionization, which are O<sup>+3</sup>, N<sup>+2</sup>, and C<sup>+1</sup>. Odegard & Cassinelli (1982) explained the more complicated case of the Si IV lines, again using the Auger process. Soon after the predictions based on the Auger mechanism were made, X-rays were discovered from O stars in the first observations with the *Einstein* satellite (Seward et al. 1979; Harnden et al. 1979). However the observed X-ray spectral distribution did not agree with the idea that the X-rays were arising from a thin corona at the base of the cool wind, because the attenuation of soft X-rays by the cool wind was absent. It became clear that X-ray sources needed to occur farther out in the wind. Lucy & White (1982) and Lucy (1982) proposed that the X-rays were generated from shocks embedded in the wind and developed models of structured shocks. In fact, Lucy & White (1980) proposed that the shocks were at the *outer* face of clumps being driven through the wind, and thus were bow shock in nature. An advantage of the shock models is that they could form naturally by virtue of the instability in the

physics of line-driven winds (as first noted by Lucy & Solomon 1970). Thus, unlike the warm wind and the corona plus cool wind models, shocks formed by line-driven wind instabilities do not need to assume an input of mechanical energy flux from the star to heat either an extensive part of the wind or a thin coronal zone.

From a moderately high resolution spectrum of Orion belt stars with the *Einstein* satellite Solid State Spectrometer, Cassinelli & Swank (1983) found X-ray line emission from Si XIII and S XV in  $\zeta$  Ori. These indicated the presence of gas that is hotter than had been needed to explain the softer X-ray flux. Since this relatively hard line radiation could escape from deep in the wind, they proposed that there could still be zones, such as magnetic loops of very hot plasma, near the star's surface. Because single OB stars are not noted for X-ray variability at more than about the 1% level, Cassinelli & Swank also concluded that the embedded wind shocks could not be in the form of spherical shells, as in the picture of Lucy (1982), but rather there must be of order  $10^4$  distributed sources or "shock fragments" in the wind. The emission from a number of sources at a range of heights in the wind would lead to a statistically steady rate of X-ray production. Thus, even from relatively early in the history of hot star X-ray astronomy it was thought that the X-rays must arise from discrete distributed source regions, with the possibility that hotter zones are present near the star. Further improvements on that picture required the higher spectral resolution of *Chandra* and *XMM-Newton*.

The nature of the line-driven wind instability that leads to shocked regions was more fully explained by Owocki et al. (1988), who developed a radial, 1D picture for the spatial distribution of the shocks. Spherically symmetric shock models have also been computed, for example, by Cooper (1994) and Feldmeier et al. (1997). MacFarlane & Cassinelli (1989) developed a basic model for an individual shock as being in the form of a "driven wave" with an inward boundary on the starward side of the wave where the wind collides with the driven wave, and an outward facing shock at the upper boundary where the driven wave catches up with slower moving material ahead. The shock properties were explained in terms of basic Rankine-Hugoniot shock relations. The driven wave has a nearly constant pressure, set by the dynamic pressure of the incident material ( $\rho V_{\text{rel}}^2$ ), and the temperature of the gas can be quite high and is determined by  $V_{\text{rel}}^2$ , where  $V_{\text{rel}}$  is the speed of the incident material relative to the shock front. For strong shocks the density increases by a factor of 4 relative to the incident material, and then in the layers of the driven wave where the gas radiatively cools back to the radiative equilibrium value of the ambient wind, the density increases by about 3 orders of magnitude. It is likely that a shell of such a high density contrast gas is unstable, such that the compressed gas will not remain in the form of a spherically expanding shell, but instead break up into clumps with densities of about  $10^3$  times that of the ambient wind.

The initiation of our bow shock approach arose through our attempt to understand the anomalous properties of the B0.5 V star  $\tau$  Sco (Howk et al. 2000). In *Copernicus* spectra (Lamers & Rogerson 1978), the star shows unusual redshifted absorption features in the O VI and N V P Cygni lines. This could arise if there were infall of matter. In addition, *ROSAT* observations of  $\tau$  Sco showed that the X-ray spectrum is unusually hard relative to other early B stars. Howk et al. proposed that clumps form in the wind, become dynamically uncoupled from the flow and line forces, and if they have a certain range in clump mass, follow trajectories whereby they fall back toward the star. The bow shock

around the clump would account for the X-ray emission, and drag owing to the wind/clump velocity difference would be important in the clump trajectory.

The idea that hot star winds are clumpy has been especially well investigated in regards to Wolf-Rayet (WR) stars. Lepine & Moffat (1999) found that emission features seen moving across broad optical lines of He II lines can be explained as clump emission regions moving out in the winds. Hillier (1991) showed that unclumped winds of WR stars would lead to line broadening by electron scattering that is not observed. Nugis & Lamers (2000) found that the observed IR flux distribution of WR stars is better fit with clumped models. There is also evidence for clumping in the case of other early-type stars. Lupie & Nordsieck (1987) found that the position angle of polarization seen in B supergiants shows irregular changes, and they interpreted this as arising from very large density enhancements in the winds. This was perhaps the first indication of fragmentation at a *large* scale. Brown et al. (2000) showed that only large-scale concentrations of matter can lead to observable polarization changes, because smaller scale reshuffling of electrons in an envelope does not lead to a significant net polarization change. In addition to the WR and B supergiants, there is new evidence of wind clumping in O star winds (Bouret et al. 2003, 2005; Evans et al. 2004).

Clumping is important (1) because it leads to overestimates of the mass-loss rate ( $\dot{M}$ ) values of early-type stars that are derived from density square diagnostics (Abbott et al. 1981), and (2) because the downwardly revised  $\dot{M}$  values affect the X-ray spectra owing to a reduced absorption column density through overlying wind material. The best estimates of  $\dot{M}$  had long been assumed to be those derived from the free-free radio flux of stars (Barlow & Cohen 1977; Cassinelli & Hartmann 1977). The results were considered the most reliable because the free-free transitions lead to a large (LTE) opacity; the observable radio flux tends to form in the outer regions of the wind where the velocity is constant and the density  $\rho$  varies simply as  $r^{-2}$ ; and the wind temperature cancels from the emergent flux formula.

The topic of clumping has recently become a major one because surprisingly large reductions to the mass-loss rates for O stars have been suggested by Massa et al. (2003) and Fullerton et al. (2006). These authors argue that a better estimator of  $\dot{M}$  is the P Cygni profile of the P v ( $\lambda 1118, 1128$ ) doublet. This spectral feature has several advantages: it originates in a dominant ion stage, so there is a minimal ionization fraction correction and the profile is typically unsaturated in UV spectra. Also, since the line opacity depends only linearly on density, the line depth is not affected by clumping in the wind. Fullerton et al. deduce mass-loss rate reductions by at least a factor of 1/10 to 1/100 times traditional values. However, based on our clump picture, we question the idea that the clumping does not affect the abundance of the P v, because the clumps are immediately adjacent to X-ray sources, and thus the fraction of phosphorus in the observable P v stage could be reduced significantly owing to the multiple ionizations associated with the Auger effect (Odegard & Cassinelli 1982)

Another argument against the significant decrease in  $\dot{M}$  is from WC07, who find that the radii of formation of the X-ray lines correspond quite well with the values at which radial optical depth is unity when using the traditional  $\dot{M}$  values. Thus, lines from soft ions such as that of N VII (25 Å) form at 5–10 stellar radii because the opacity to radiation at these wavelengths is large. (Continuum opacity, much of it K-shell opacity of abundant

metals, varies roughly as  $\lambda^3$ .) Shorter wavelength lines, that originate from the higher ions, such as Ne IX, Mg XI, and Si XIII, can be seen as forming progressively deeper. These are also near their respective optical depth unity locations, if traditional  $\dot{M}$  values are used. Another good argument against the drastic decrease in the mass-loss rates is that it would affect the well-established results of massive star evolution (Hirschi 2007). The topic of clumping is an active one, and at the recent Potsdam international workshop on hot star wind clumps (Hamann et al. 2007), a consensus was reached that  $\dot{M}$  could not be reduced by more than about a factor of 3 from the traditional values.

In summary, it has become important to understand the properties and the effects of clumps in winds. Our plan here is to consider the various effects discrete clumps would have on observations of X-ray lines and to establish an analytical tool to interpret observations. There is evidence for clumps being important in astrophysics in general, for example, bow shocks also appear in images of Herbig-Haro objects (e.g., Eisloffel et al. 1994) and planetary nebulae (O'Dell & Handron 1996). By using *Chandra* data we can obtain good information on the clumps in hot star winds.

In § 2 we summarize some of the problematic X-ray results obtained from *Chandra*. In § 3 we describe the numerical method we have used and show the most relevant results regarding the post shock temperature and density structure, as well as the temperature distributed emission measure. In § 4 the bow shock structure is contrasted with plane parallel shock pictures and in § 5, we develop a simple “on the shock” approximation to provide some insight regarding bow shocks. In particular, we give a derivation of the distributed emission measure power law with temperature and discuss the angular flow around the clump. Overall conclusions are summarized in § 6.

## 2. HOT STAR X-RAY PROBLEMS

At the forefront of current problems in this field is the finding that X-ray line profiles from massive star winds are quite different from what had been expected. MacFarlane et al. (1991) had predicted that lines formed by shocks in stellar winds should be blueshifted and skewed. This is because the shock regions on the far side of the star (where the gas is red shifted) would be more highly attenuated by bound-free continuum opacity of the wind matter by virtue of being at higher column density relative to the observer. This effect was below the spectral resolution of the emission lines of the two B stars ( $\epsilon$  CMa and  $\beta$  CMa) that were observable with the *Extreme Ultraviolet Explorer (EUVE)* satellite. These stars were observable at 70–730 and 500–700 Å, respectively (Cassinelli et al. 1995, 1996). However, well-resolved line profiles at the even shorter X-ray wavelengths are observable with the high-energy and medium-energy grating spectrometers (HEG and MEG) on *Chandra*. The *Chandra* observations (Waldron & Cassinelli 2001; Miller et al. 2002; Leutenegger et al. 2006; WC07) do not show the expected blueward skewing of the lines nor blueshifting of the line centroids. The lines also tend to be broad, although much narrower for the low-luminosity classes of hot stars, and for all luminosity classes the HWHM is less than the terminal wind speed. This problem of symmetry alone has motivated several ideas.

1. If the mass-loss rates were reduced by an order of magnitude or more, the winds would be sufficiently thin that radiation from both the near *and* far side could escape (Cohen et al. 2006; Leutenegger et al. 2006).

2. Owing to clumps, the winds could be more porous to the transfer of X-rays (Oskinova et al. 2006). The presence of high-density fragments allows the X-rays to escape from deeper in the wind, and one could detect sufficient X-rays from the far side of the star to eliminate the net shifting and skewing effects.

3. There is enhanced Sobolev escape of line radiation out the side of shocks (Ignace & Gayley 2002). This means that the line radiation is coming in large part from the “sides” of the star, as seen by the observer, and this occurs where the radial flow has a small line-of-sight velocity. Although we are not employing the Sobolev escape argument, we find the enhanced sideways escape to be a useful concept.

In the study of clump effects by Feldmeier et al. (2003) and Oskinova et al. (2004), the clump regions are pictured to be in the form of plane parallel slabs. These correspond to regions of enhanced absorption of the X-rays that originate in broader, more diffuse wind regions. WC07 note that the derived radii of the line-source regions found by these authors are larger than the rather small radii that WC07 find from an analysis of the forbidden-intercombination-resonance (fir) lines of He-like ions. Oskinova et al. (2004) have developed plausible explanations for the unshifted unskewed lines that are observed in  $\zeta$  Ori. The clumps, in their view, arise from a runaway effect first described in Feldmeier et al. (1997). Whether porosity at the required level can explain the observations has been questioned by Owocki & Cohen (2006). Nevertheless, the Oskinova et al. picture combines several elements: the fragmentary nature of shocks and the possibility of producing X-rays at a range of radii that is needed in any explanation of hot star X-rays.

## 3. A HYDRODYNAMIC CALCULATION OF A WIND COLLIDING WITH AN IMPENETRABLE OBJECT

We use the magnetohydrodynamic (MHD) code that was developed by Cho & Lazarian (2002) to model the bow shock that forms from a plane-parallel flow impinging on a spherical blunt obstacle. As a first step in understanding the effects of bow shocks on hot star X-ray emission, we choose to assume that the clump is impenetrable. Actual clumps are likely to be more complicated, and the clumps could have a highly time-dependent interaction with the incident wind. However, to ensure that we are not dealing with numerical noise phenomena, we treat the simplest case possible as a starting point for our theoretical exploration of bow shock effects. The main expectation is the formation of a bow shock around the clump that exhibits a range in hot plasma temperatures along with a nontrivial vector velocity flow. This recipe is suggestively promising for explaining the observed X-ray spectral features from hot stars.

For the simulation, the clump is assumed to be stationary and spherical with a radius  $R_c$ . The incident flow is plane-parallel at constant speed and is parameterized by the mass flux and flow speed. In such an idealized case, the X-ray emission arises owing to the postshock gas that envelops the clump. All of the emission arises *from the wind matter* that is heated, compressed, and re-directed at the bow shock interface. For the purpose of interpreting X-ray observations, we are interested in finding the temperature and density structure, and the distributed emission measure. Using these physical properties in conjunction with a cooling function provides the X-ray emissivity of a blob as a function of wavelength and the line profile emission for a particular transition of interest.

TABLE 1  
BOW SHOCK SIMULATION PARAMETERS

Simulation Parameter	Value(s)
$R_c$ (cm).....	$10^{10}$
(Mach No.) $_W$ .....	47 and 71
$V_W$ (km s $^{-1}$ ).....	1000 and 1500
$N_{W,e}$ (cm $^{-3}$ ).....	$10^{10}$
$T_W$ (K).....	$2 \times 10^4$
$T_A$ (K).....	$1.4 \times 10^7$ and $3.2 \times 10^7$
$\rho_W V_W^2$ (dyne cm $^{-2}$ ).....	100 and 233

For computing the structure from bow shocks, we use a third-order hybrid essentially nonoscillatory (ENO) MHD routine as described in Cho & Lazarian (2002) and references therein to reduce spurious oscillations near shock; two ENO schemes are combined. When variables are sufficiently smooth, the third-order weighted ENO scheme is used without characteristic mode decomposition. When the opposite is true, the third-order convex ENO scheme (Liu & Osher 1998) is used. A three-stage Runge-Kutta method is employed for time integration. The ideal MHD equations are solved with the magnetic field set to zero everywhere. The simulation runs until it reaches an approximately steady state bow shock, usually after about two wind crossing times owing to the highly hypersonic nature of the flow. The simulations reported in this paper are axisymmetric. We adopt cylindrical coordinates  $(\varpi, \phi, z)$  with incident flow moving in the  $+z$ -direction, so the bow shock is axisymmetric about the  $z$ -axis. We frequently refer to the transverse coordinate  $\varpi$  as the impact parameter. Some early results were presented by Moeckel et al. (2002).

In the calculations a polytropic relation with  $P \propto \rho^\gamma$  is assumed so that the temperature structure is determined by the expansion cooling of the gas after it passes through the bow shock geometry. Adiabatic cooling is an appropriate approximation for the case of high-velocity inflow, so the postshock region is at a high temperature where radiative losses are less important than expansion. The computed results for the shape of the shock are quite similar to the semianalytic results of Lomax & Inouye (1964) for a  $\gamma = 5/3$  bow shock.

The incident velocity is specified as a Mach number  $M_W$ , and here we present the results of an analysis of an adiabatic bow shock with wind flow  $M_W = 47$  and 71, that correspond to relative velocities of 1000 and 1500 km s $^{-1}$ , respectively. Throughout this paper, the subscript “ $W$ ” refers to wind properties. A fast wind is assumed to be incident on a rigid stationary sphere, creating the bow shock structure. The sphere has a radius of 32 grid points. The center of the sphere was located one half grid spacing below the lowest grid point. The results of this simulation are robust for other large values of  $M_W$  since the shock shape, flow pattern, and shock structure are all nearly independent of Mach number in the hypersonic limit of  $M_W \gg 1$  for an adiabatic case (Hayes & Probstein 1966). The parameters used in our simulations are given in Table 1.

The most basic parameters for determining the structure of a bow shock around a blunt object are the incident velocity, which determines the postshock temperature, and the incident mass flux  $\rho_W V_{\text{rel}}$ . The numerical calculation is made in the rest frame of the rigid sphere where  $V_{\text{rel}}$  is the difference between the radial wind velocity and the radial clump velocity. The postshock gas temperature follows the well-known Rankine-Hugoniot relation between the velocity perpendicular to the shock and the postshock temperature. The maximum temperature,  $T_A$  achieved occurs at

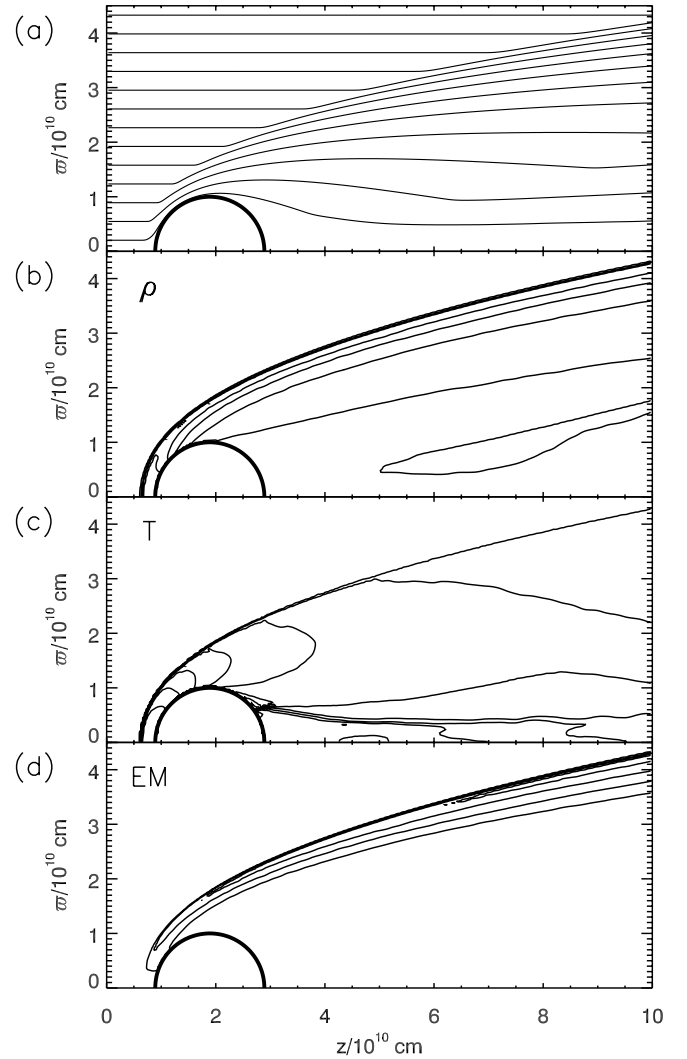


FIG. 1.—Simulation results of an adiabatic bow shock forming in response to an impenetrable sphere using the parameters given in Table 1 with  $V_W = 1500$  km s $^{-1}$ . Shown are (a) flow streamlines; (b) density with contours at 0.4, 1.2, 2.0, 2.8, and 3.6 times  $N_W$ ; (c) temperature with contours at 1, 2, 6, 10, 15, 21, and 28 MK; (d) emission measure contours of  $2\pi\varpi N^2$  separated by factors of 2, with the largest value at  $2.44 \times 10^{22}$  cm $^{-5}$  and showing that the emission measure is isolated strongly at the shock front.

the “apex” of the bow shock (i.e., along the line of symmetry) and is given by

$$T_A = \frac{3}{16} \frac{\mu m_H}{k} (V_{\text{rel},\perp}^2) \quad (1)$$

$$= 14 \text{ MK} \left( \frac{V_{W,\perp}}{1000 \text{ km s}^{-1}} \right)^2, \quad (2)$$

where in the latter expression we have evaluated the constants using fully ionized solar abundances and  $\mu = 0.62$ , and  $V_{W,\perp}$  is the perpendicular speed of the preshock gas relative to the shock front.

Figure 1 shows simulation results from our adiabatic bow shock case using the parameters listed in Table 1. Figure 1 shows the streamlines of the flow (panel a), the density (panel b), temperature (panel c), and emission measure distributions (panel d). Figure 2 shows temperature contours behind the bow shock superposed with vectors detailing the postshock flow velocity. Note especially the decreasing temperature along the bow shock

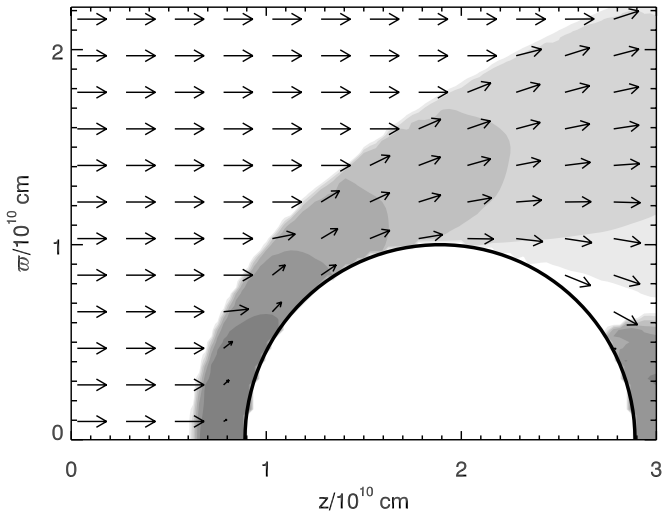


FIG. 2.—Contour plot of temperature in the bow shock simulation. The peak temperature contour value near the stagnation region is  $T_A$  given by eq. (2), and the contours in temperature have the same spacing as in Fig. 1. Arrows show the velocity vectors.

with distance from the apex, and also that the flow of gas around the clump leads to a significant transverse vector velocity field in conjunction with the temperature distribution. Note also that all the X-ray emission properties, in which we have special interest here, closely hug the bow shock surface. This is what inspires our introduction of the “on the shock” (OTSh) approximation. In the following section we consider observables relating to these properties of the clump-wind simulation.

#### 4. THE TEMPERATURE DISTRIBUTION OF THE EMISSION MEASURE

##### 4.1. Results for a Single Clump

An important property for understanding processes that generate hot plasma in astrophysical sources is the temperature distribution of the emission measure. This distribution is often called the “differential emission measure,” but the use of this term in the X-ray literature is not uniform, and we prefer simply to refer to the temperature distribution of the emission measure or  $EM(T)$ . The contribution to the emission measure at a given temperature range from  $T$  to  $T + dT$  can arise from totally disconnected regions in the X-ray-emitting region. The volume emission measure (EM) is defined as

$$EM = \int N_e N_p dV, \quad (3)$$

a volume integral involving the product of the electron and proton number densities  $N_e$  and  $N_p$ . Wojdowski & Schulz (2004, 2005, hereafter WS04 and WS05, respectively) find the amount of hot plasma at each range in temperature to be a decreasing power law for most hot stars, with the exception of those few hot stars known to possess highly magnetized envelopes (e.g.,  $\theta^1$  Ori C; see Donati et al. 2002). Each of the X-ray emission lines is associated with a range of temperatures that can be found from the APEC software (Smith et al. 2001). From the strength of the line, Wojdowski & Schulz find the interesting result that  $EM(T)$  is a downward-sloping power law extending from about 2 MK, up to an apparent maximum that is

TABLE 2  
EMISSION MEASURE SLOPES VERSUS TEMPERATURE

Star	Spectral Type	Slope $p$ ( $= 1 + d \log EM/d \log T$ )
$\zeta$ Pup .....	O4f	-1.1
$\zeta$ Ori .....	O9.7 Ib	-1.2
$\iota$ Ori .....	O9 III	-1.3
$\delta$ Ori .....	O9.5 II	-0.9
HD 206267 .....	O6.5 V	-2.2
$\beta$ Cru .....	B0.5 III	-2.1
$\tau$ Sco .....	B0.2 V	-0.6
$\theta^1$ Ori C .....	O4-6p	+1.5

typically about 20 MK. Such a distribution holds for the majority of the stars that were analyzed. For stars known to be highly magnetic, the  $EM(T)$  distribution can have a very different shape. The highly magnetic star  $\theta^1$  Ori C even has a positive slope over the whole temperature range, indicating the presence of larger amounts of increasingly hot material. Clearly such a distribution would have to stop at some high temperature, although this is not seen in the  $\theta^1$  Ori C plots shown by WS04 or WS05. Table 2 lists values of the  $EM(T)$  power-law index for several OB stars as derived from the analyses of WS04 and WS05.

Using the hydrodynamical code, we obtain a power-law emission measure distribution  $EM(T) \approx 10^{51.4} \text{ cm}^{-3} \times (T/T_A)^p$ , shown in Figure 3, where  $p$  is approximately  $-4/3$ . Note that the dropoff at low temperatures is an artifact of the calculation that arises from the fact that the grid in the impact parameter direction is truncated at some  $y_{\text{max}}$ . When this maximal impact parameter is increased the slope continues to follow the  $-4/3$  slope to lower temperature values. With this power-law distribution, the temperature gradient  $dEM/dT \propto T^{p-1} \propto T^{-7/3}$ , a result we use later on. This figure was obtained by binning the emission measure results of each simulation volume element into temperature cells of 0.1 in  $\log T$ .

It is useful to have the following scaling of the results of the simulations to parameters for a different clump: with radius  $R$ ,

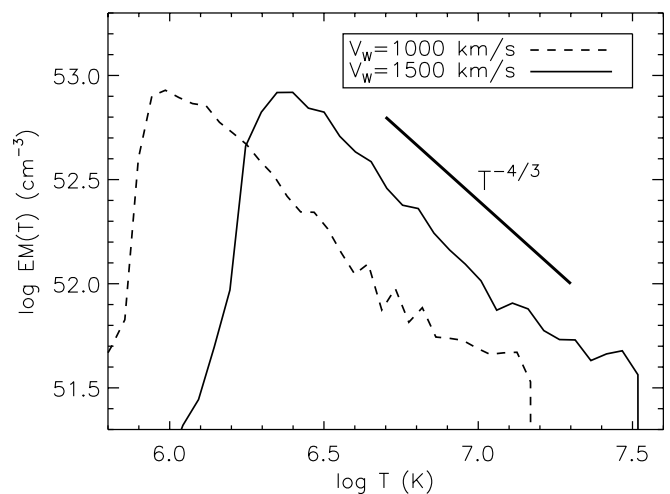


FIG. 3.—Temperature distribution of the emission measure from a simulation of an adiabatic bow shock using the parameters given in Table 1. The maximum temperature  $T_A$  is set by the speed of the incident wind relative to the shock. The low-temperature cutoff is due to the finite size of the simulation grid. The dashed line is a power-law approximation with a slope of  $-4/3$ . Two results are shown: these have  $M_W = 47$  and  $71$ , which correspond to  $V_{\text{rel}} = 1000$  and  $1500 \text{ km s}^{-1}$  as indicated

relative wind/clump velocity  $V_W$ , wind density  $N_W [= (N_e N_p)^{1/2}]$ , and apex temperature  $T_A$ . We derive the scaling

$$\text{EM}(T)/10^{51.4} \text{ cm}^{-3} \times \left(\frac{R}{R_s}\right)^3 \left(\frac{V_W}{V_s}\right)^2 \left(\frac{N_W}{N_s}\right)^2 \left(\frac{T_A}{T}\right)^{4/3} \left(\frac{\Delta \log T}{0.1}\right), \quad (4)$$

where  $V_8$  is the incident speed in  $10^8 \text{ cm s}^{-1}$ . Here we have used subscript  $s$  for our simulation results. The  $p = -4/3$  slope in Figure 3 somewhat underestimates the emission from the highest temperature bin in the distribution (by a factor of about 2), and we discuss this later in our analytic derivation of the  $d\text{EM}/dT$  relation.

From an interpretational perspective, the most important feature to note about the power law is that there is significantly more gas at low temperatures than at the high temperatures near the apex of the shock. The increasing emission measure for the lower temperatures (and hence the lower ion stages) arises from the fact that a bow shock has an increased area toward the wings where the shock is increasingly oblique. As a result of the power-law distribution  $\text{EM}(T)$ , clumps that are deep in a wind can produce a great deal of low ion emission, say, at O VII. In the case of stars with high mass-loss rates, such as Of stars and OB supergiants, the wind opacity can substantially block this emission from direct observations.

The stars that have been studied most intensively in the history of wind theory and hot star X-ray astronomy are  $\zeta$  Ori and  $\zeta$  Pup, and both have  $\text{EM}(T)$  slopes reasonably close to the  $p = -4/3$  value. However, some stars, such as  $\tau$  Sco, have a very shallow but negative slope. It has recently been discovered that this particular star is also one with a strong magnetic field (Donati et al. 2006); thus, it is likely that this star has a combination of X-rays from both the clump regions and the positive sloping  $\text{EM}(T)$  magnetic regions. Sorting the contributions from each could be difficult; however, it appears that the  $\text{EM}(T)$  analyses can yield valuable new information about clump properties and may also provide an indicator of fields in stars that have not yet shown measurable Zeeman effects. We have found a case of a positive sloping  $\text{EM}(T)$  in our recent calculations of X-rays from Be stars (Li et al. 2007) using a magnetically torqued disk model for Be stars. This model is based on the idea that the matter that enters a Be star disk is from a wind that has been channeled by a dipolar magnetic field and which is corotating with the star (Cassinelli et al. 2002; Brown et al. 2004). Higher temperature gas originates farther from the star, since the impact of the wind with the disk is at a higher speed. In this example there is a maximum to the  $\text{EM}(T)$  distribution that is directly related to the magnetic field at the base of the wind. Next we consider the consequences of having a large number of clumps contributing to the  $\text{EM}(T)$ .

#### 4.2. Ensemble of Clumps

An inspection of the results from WS05 reveals that, except for the magnetically dominated star  $\theta^1$  Ori C, observed  $\text{EM}(T)$  distributions have negative power-law slopes. However, the values are not exactly the  $-4/3$  that we derive from the clump simulation. This can arise for several reasons. The first one has already been discussed, namely some stars are strongly magnetic and those fields can dominate the  $\text{EM}(T)$  following physics that is quite distinct from clump bow shocks, and so the results are not surprisingly quite different. However, the star HD 206267A [O 6.5 V(f)] has a slope that is steeper than the  $-4/3$  value. In

WC07 we found that for near-main-sequence stars, one could detect source emission coming from a wide range in depths as the winds are not as optically thick as those in the supergiants. Thus, a second way to explain a deviation from a  $-4/3$  slope in the case of steeper  $\text{EM}(T)$  is to consider the X-rays as arising from an ensemble of different clumps.

Such an ensemble does not represent only more or fewer clump bow shocks but in fact a range of  $T_A$  values. Each individual clump contributes a  $\text{EM}(T)$  distribution of slope  $-4/3$  for  $T < T_A$ , but now clumps exist at different radii, and thus a range in  $T_A$  may plausibly exist from a range in  $V_{\text{rel}}$  values. The consequence of staggered values in  $T_A$  leads naturally to a slope that is steeper than  $-4/3$ . All clumps contribute to low-temperature plasma, but only a small minority contribute to the absolute maximum temperature achieved in the entire wind. Note that one way to provide an observational cutoff for lower temperatures is to recognize that even rather low mass loss winds will eventually lead to substantial photoabsorption at sufficiently low X-ray energies. Second, our simulation assumes the clump is small compared to the radius of the star, such that the wind is plane parallel on the scale of the clump size. However, the stellar wind is in fact spherically divergent, and so the flow striking the a large bow shock is actually more oblique than is achieved in the plane-parallel flow simulation.

#### 4.3. Adiabatic and Radiative Cooling Regions

Before leaving the topic of  $\text{EM}(T)$ , it is important to comment on the applicability of the adiabatic assumption. Across a bow shock there is a large range in temperatures, and even if the adiabatic assumption holds near the apex of the shock, it will fail somewhere out in the wings, since radiative cooling is extremely efficient for  $T < 10^6$  K. So it is relevant to consider the regimes in which the cooling time is small or large compared to the flow time in the simulation.

Adiabatic cooling is a result of expansion cooling as the flow navigates around the clump. Throughout this trajectory the gas is emitting X-rays, and so the gas is cooling by radiation as well; however, the adiabatic assumption adopted in our hydrodynamical simulation will apply to those cases when the radiative cooling timescale is slow relative to expansion cooling.

To characterize the comparison, we define  $t_{\text{flow}}$  as the flow timescale associated with adiabatic cooling. This will scale as  $t_{\text{flow}} \approx R_c / V_{\text{rel}}$ . With  $R_c = 10^{10}$  cm and a wind speed of  $500 \text{ km s}^{-1}$  (approximately a quarter of the terminal speed for a typical O star wind), the flow time works out to  $t_{\text{flow}} \sim 10^3$  s. We define the radiative cooling time with  $t_{\text{rad}}$ , which can be estimated as the ratio of the thermal energy density  $U_{\text{th}}$  to the cooling rate  $dU/dt$ . Thus,  $t_{\text{rad}} \approx U_{\text{th}} / (dU/dt) = (N_e kT) / [\Lambda(T) N_e^2]$ , where  $\Lambda$  is the cooling function in  $\text{erg cm}^3 \text{ s}^{-1}$ , which is tabulated in Cox (2000), giving the result  $\log \Lambda = -21.6 - 0.6(\log T - 5.5)$ . At a value of  $T = 10^7$  K associated with  $T_A$  and a number density of  $N_e = 10^{10} \text{ cm}^{-3}$ , the radiative cooling time becomes  $t_{\text{rad}} \sim 10^4$  s, about 10 times larger than the flow timescale under these conditions.

Clearly, the radiative cooling is dominant over adiabatic cooling where the wind density is large or the shock temperature is low, and in future simulations it will be important to include radiative cooling. However, it is still useful to consider the limiting case of adiabatic cooling. First, although 1D simulations show radiative cooling to be important, expansion cooling is there limited to  $r^{-2}$  divergence, and shock structures are necessarily spherical shells in these simulations, which we know not to be true based on low levels of X-ray variability (Cassinelli & Swank 1983). Our 2D simulations allow for a new geometric avenue of expansion cooling because of the channeling of the gas around the

clump in the form of a bow shock, thus requiring a new assessment of how adiabatic cooling contributes to the interpretation of hot star X-rays. Second, in the hypersonic limit, the results for pure adiabatic cooling are quite robust because the bow shock shape and temperature distribution are independent of density. This is not the case for radiative cooling, hence one expects the radiative bow shock properties to be different for clumps at different radii in the wind. And third, as discussed in the preceding section, we can explore the extent to which this limiting case can reproduce observed differential emission measure distributions. Departures from the model predictions are suggestive of contributions by radiative cooling or other effects, such as stellar magnetism.

### 5. THE “ON THE SHOCK” APPROXIMATION

From the numerical modeling, we find, in contrast with planar shocks (e.g., Feldmeier et al. 1997), that the X-ray emission is dominated by a zone lying just behind the shock front (as seen in Fig. 1*d*). Hence, we introduce the OTSh approximation for a simple analysis of bow shocks. In the case of planar frontal shocks, the postshock flow must continue in a straight line, and thus the only cooling that occurs is radiative emission. In the case of a bow shock, there is always an expansion of the gas around the sides of the clump and is associated with adiabatic cooling.

Consider a simple but useful picture for the shock structure. As before, let the  $z$ -axis be the radial direction from the star through the apex of the shock and through the center of the spherical clump. Let  $\varpi$  be the perpendicular direction that corresponds to the impact parameter of the wind flow relative to the center of the clump. The shape of the bow shock from our simulation can be fit with a power-law curve given by

$$\frac{z - z_0}{R_c} = a \left( \frac{\varpi}{R_c} \right)^m, \quad (5)$$

with  $a = 0.35$  and  $m = 2.34$ , hence a shape not far from a parabola. This provides a good fit out to  $\varpi \sim 5$  clump radii. An exact solution to the shock shape derived using an inverse method is given in Lomax & Inouye (1964), and our result for the shock shape agrees well with theirs. Their paper does not provide the temperature and emission measure information of special interest to us. In addition to the shape, it will also be useful to know the derivative of the shape (i.e., the position-dependent tangent). We define this to be  $g(\varpi) = \tan A_1 = dz/d\varpi$ , where  $A_1$  is the angle that the incident wind makes relative to the bow shock.

#### 5.1. Postshock Velocity Components

Figure 4 shows a postshock (hereafter identified with subscript “P”) flow trajectory associated with crossing the bow shock. The jump conditions for the velocity components perpendicular and parallel to the shock front are

$$V_{P,\perp} = \frac{1}{4} V_{W,\perp}, \quad (6)$$

$$V_{P,\parallel} = V_{W,\parallel}. \quad (7)$$

All across the face of the shock the incident wind speed is given by  $\mathbf{V} = V_W \hat{e}_z$ . Based on the geometry of Figure 4 we can derive the following relations:

$$V_{W,\perp} = V_W \cos(A_1) = V_W \frac{1}{\sqrt{1+g^2}}, \quad (8)$$

$$V_{W,\parallel} = V_W \sin(A_1) = V_W \frac{g}{\sqrt{1+g^2}}, \quad (9)$$

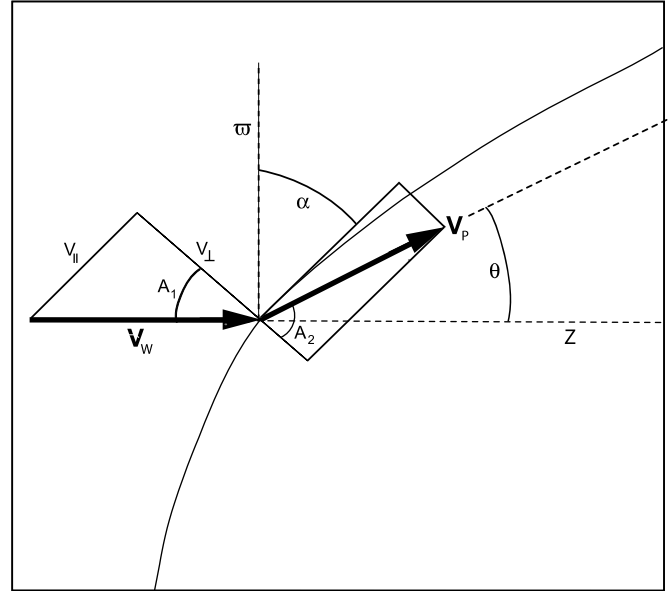


FIG. 4.—Illustration of the changes in velocity components at the shock front. The angles  $A_1$  and  $A_2$  are the incident and emergent angles of the flow relative to the direction perpendicular to the bow shock, and  $\theta$  represents the angle between the postshock velocity vector and the  $z$ -direction. The impact parameter of a streamline is given by its  $\varpi$  coordinate value.

where we have expressed the velocity quantities in terms of the shape gradient  $g(\varpi)$ . The following limiting behavior is implied: as  $g \ll 1$ , the wind is essentially normal to the shock as occurs along the stagnation line, and at large impact parameter where  $g \gg 1$ , the shock becomes nearly parallel to the incident wind flow.

Consider a jump that occurs at some position on the shock ( $\varpi, z$ ). The incident wind speed  $V_W$  relative to the orientation of the shock front can be expressed as  $V_W^2 = V_{W,\perp}^2 + V_{W,\parallel}^2$ . The total postshock velocity is  $V_P^2 = (V_{W,\perp}/4)^2 + V_{W,\parallel}^2$ , which on using substitution using the relations (8) and (9) becomes

$$V_P^2 = V_W^2 \frac{1/16 + h_1^2}{1 + h_1^2}, \quad (10)$$

where on the postshock side, the velocity vector makes an angle relative to the normal implicitly defined by  $h_1 \equiv \tan A_2 = V_{P,\perp}/V_{P,\parallel} = 4 \tan A_1$ . Thus,

$$V_{P,\perp} = V_P \cos A_2 = V_P \frac{1}{\sqrt{1+h_1^2}}, \quad (11)$$

$$V_{P,\parallel} = V_P \sin A_2 = V_P \frac{h_1}{\sqrt{1+h_1^2}}. \quad (12)$$

#### 5.2. Temperature Distribution across the Bow Shock

The postshock temperature as a function of impact parameter  $\varpi$  is related to the change in the perpendicular velocity component as described in the previous section. The temperature distribution is given by

$$T_P(\varpi) = \frac{3}{16} \frac{\mu m_H}{k} (\mathbf{V} \cdot \hat{e}_n)^2 \quad (13)$$

$$= T_A \cos^2(A_1)$$

$$= \frac{T_A}{1 + g^2(\varpi)}, \quad (14)$$

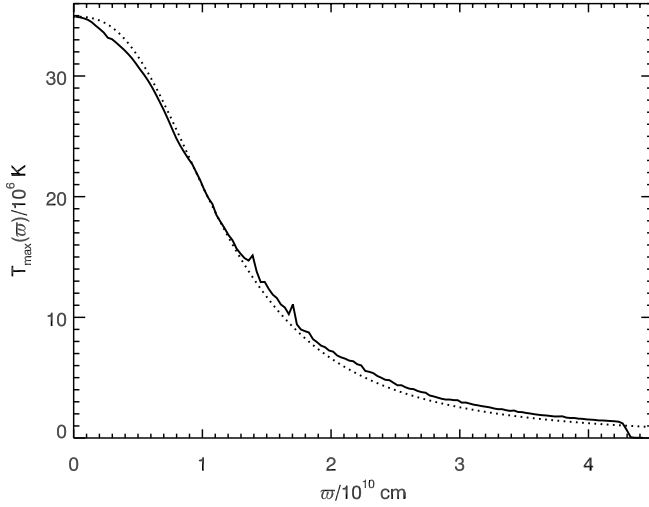


FIG. 5.—Maximum temperature as a function of impact parameter in our simulation of an adiabatic bow shock. Shown are simulation results (*solid line*) and eq. (16) (*dotted line*).

where  $T_A$  is the highest temperature gas, at the bow shock apex. Thus, we see that each impact parameter point on the shock has a specific postshock temperature associated with it, hence formally  $\varpi = f(T)$ . The simple power law for the bow shock geometry in equation (5) leads to

$$\frac{dz}{d\varpi} \equiv g(\varpi) = am(\varpi/R_c)^{m-1}; \quad (15)$$

thus, we get an explicit equation for temperature in the OTSh approach:

$$\frac{T}{T_A} = [1 + g^2]^{-1} = \left[ 1 + 0.67 \left( \frac{\varpi}{R_c} \right)^{2.68} \right]^{-1}. \quad (16)$$

This expression is plotted against the maximum temperature along an impact parameter in Figure 5, where the agreement between the model and the preceding expression is remarkably good. This close agreement is related to the conditions of the simulation being hypersonic.

### 5.3. Polar Angle Distributions of the X-Rays

To facilitate the use of these results for evaluating observables from an ensemble of clumps, such as in predicting emergent line widths, it is convenient to express the angles of the inflow and postshock flow relative to the local “radial” (or  $z$ ) direction. This is a blob-centered  $(r, \theta, \phi)$  system. The incident radial wind flow has  $\theta_{\text{in}} = 0^\circ$ . On the postshock side, the angle is  $\theta_P = A_2 - A_1$ , hence the stream flow emerges from the bow shock at

$$\tan \theta_P = \frac{3g}{1 + 4g^2} \equiv h_2. \quad (17)$$

Thus, the “transverse” or sine component of the postshock velocity vector is  $\sin \theta_P = h_2/(1 + h_2^2)^{1/2}$ .

What is particularly interesting about the postshock velocity and its direction is that it affects the observed line profiles. The

postshock speed can, for example, have a rather large transverse value, as illustrated in Figure 2. To choose one case as an example, consider the one-angle quadrature value of Lucy & White (1980):  $A_1 = 30^\circ$ , then  $A_2 = 67^\circ$ ,  $V_P = 0.56V_W$ , and the transverse component of the postshock velocity is one-third of  $V_W$ . This is already a significant fraction of observed X-ray line widths (in WC07 this was typically about  $0.4V_W$ ). In a simulation involving many clumps, one would need to account for the line-of-sight velocity of each of the clumps. The narrower lines found by WC07 for the near-main-sequence stars and for the lower ion stages can be explained by having the line formation regions being closer to the star, where the local wind speed is smaller than is the case for the supergiants. For the latter case the radiation must arise from regions above about optical depth unity, and this is well out in the wind, where the wind speed is near the fast terminal speed.

The transverse component of the X-ray-emitting matter is another significant difference from planar shocks. The planar shocks are usually assumed to be perpendicular to the flow, and thus the postshock matter continues flowing only perpendicular to the shock front.

### 5.4. Temperature Distributions of the Emission Measure

Semianalytic expressions for bow shock properties have been derived before, especially for the simple case that we consider here in which the compact object is an impenetrable sphere. For example, Canto & Raga (1998) derived the shock shape and pressure density structure for an isothermal bow shock. This is valid for cases in which the cooling time is rapid and so the shock material forms a thin sheet around the blunt object. In contrast, our specific interest is in the hot adiabatic region where the X-ray emission originates.

Our results for the postshock density have motivated our OTSh approximation that provides a temperature, velocity, and EM from each spatial element of the bow shock surface. These are useful for understanding some of the outstanding questions raised by high spectral resolution X-ray data (e.g., Burke et al. 2006). In a separate paper, the OTSh approximation will be employed in quantitative spectral synthesis to model X-ray line profile shapes. Here, we present a derivation for  $EM(T)$  to show that the power-law temperature distribution arises naturally from the bow shock geometry.

Based on our hydrodynamic simulation, the OTSh approximation asserts that the hot gas contributing to EM closely hugs the bow shock surface. In this region the density is nearly constant at  $N = 4N_W$  everywhere along the bow shock. Hence, the volume element,  $dV$ , associated with  $dEM$  must scale roughly as the incremental surface area  $dS$  of the bow shock times some depth parameter which we call  $\Delta\ell$ . This  $\Delta\ell$  parameter represents a characteristic depth that is perpendicular to the bow shock surface. Then our expression for  $dEM$  is given by

$$dEM = N^2 dS \Delta\ell. \quad (18)$$

The differential surface area for any function  $\varpi = f(z)$  used for a surface of revolution about the  $z$ -axis is given by

$$dS = 2\pi\varpi \left[ 1 + \left( \frac{d\varpi}{dz} \right)^2 \right]^{1/2} dz. \quad (19)$$

Recalling that  $g = dz/d\varpi$ ,  $T/T_A = (1 + g^2)^{-1}$ , and defining  $\tau = T/T_A$ , the rate change in surface area with the monotonic temperature “coordinate” along the surface becomes

$$\begin{aligned} \frac{dS}{dT} &= 2\pi\varpi \left(1 + \frac{1}{g^2}\right)^{1/2} \frac{dz}{dT} \\ &= 2\pi\varpi \frac{\sqrt{1 + g^2}}{g} \frac{dz}{d\varpi} \frac{d\varpi}{dT} \\ &= \tau^{-1/2} \left(2\pi\varpi \frac{d\varpi}{d\tau}\right) \\ &= \tau^{-1/2} \frac{d}{d\tau} (\pi\varpi^2). \end{aligned} \quad (20)$$

This rather elegant result requires yet one more step to fully determine the surface gradient entirely in terms of temperature; that step requires the solution to  $\varpi(T)$ . The mapping between  $\varpi$  and  $T$  is made through the factor  $g$  using equations (5) and (16), yielding the implicit relation of

$$g = am \left(\frac{\varpi}{R_c}\right)^{m-1} = \sqrt{\frac{1}{\tau} - 1}. \quad (21)$$

Solving for  $\varpi$ , taking the gradient with temperature, and doing some algebraic manipulation yields finally

$$\begin{aligned} \frac{dS}{d\tau} &= -\pi R_c^2 (am)^{-2/(m-1)} \tau^{-(3m-1)/(2m-2)} \\ &\quad \times (1 - \tau)^{-(m-2)/(m-1)}. \end{aligned} \quad (22)$$

We know that the result of the simulation for the emission measure is  $dEM/dT \propto T^{-7/3}$ , and we know that the value of  $m$  for the bow shock is only a little steeper than a parabola. Using equations (18) and (22), it is convenient therefore to express the final result for the emission measure gradient as

$$\frac{dEM}{dT} = -\frac{\pi N^2 R_c^2 \Delta \ell}{(am)^{2/(m-1)} T_A} \tau^{-2.5+\alpha} (1 - \tau)^{-\alpha}, \quad (23)$$

where  $\alpha = (m - 2)/(m - 1)$ . If the bow shock were exactly a parabola, then  $m = 2$ ,  $\alpha = 0$ , and  $dEM/dT \propto T^{-2.5}$  is a pure power law with an exponent remarkably close to the value of  $-7/3 = -2.33$ . With  $m = 2.34$  and  $\alpha = 0.25$ , the OTSh approximation predicts an emission measure gradient of  $dEM/dT \propto T^{-2.25} (1 - \tau)^{-0.25}$ . In the limit that  $T \ll T_A$ , we have that  $\tau \ll 1$  and  $dEM/dT$  is again a power law with an exponent that is now even closer to the fit value. Obtaining an exact match to the fit exponent of the simulation requires  $m = 2.20$  in the low  $\tau$  limit, not far from the  $m = 2.34$  value derived from the bow shock shape. It would appear then that the OTSh is an excellent approximation for the emission measure and temperature distributions of the bow shock in the hypersonic and adiabatic limits.

There is one problem with equation (23) in that near the bow shock apex,  $\tau$  approaches unity, in which case  $dEM/dT$  becomes singular for  $\alpha > 0$ . This singularity is, however, only a mathematical artifact. The cusp arises from our fit to the  $z(\varpi)$  formula with a power-law exponent of 2.34, but in fact the analytic result of Lomax & Inoye indicates that very near the apex the curve is a parabola, in which case  $dEM/dT$  is nonsingular. Earlier we noted that the  $p = -4/3$  law underestimates the EM very close to the apex temperature. It is interesting that the parameterization of equation (23) does lead to a rise in  $EM(T)$  when  $\tau$  is not

negligible. In practice, the singularity can be avoided by applying a high-temperature cutoff, in which case the OTSh provides an excellent prescription for  $z(\varpi)$ ,  $T(\varpi)$ , and  $EM(T)$ .

With regards to the  $\Delta \ell$  factor, based on the simulations, achieving the good results for  $dEM/dT$  in terms of  $S(T)$  means that the range of constant density along the bow shock is consistent with  $\Delta \ell$  at a constant width. We find a value of  $\Delta \ell \approx 0.1 R_c$ , independent of the  $y$ -location along the bow shock. It is now useful to define an emission measure scaling parameter  $EM_0$ , using  $a = 0.35$  and  $m = 2.34$ , giving

$$\begin{aligned} EM_0 &= \frac{\pi N^2 R_c^2 \Delta \ell}{(am)^{2/(m-1)}} \\ &= 6.8 \times 10^{51} \text{ cm}^{-3} \left(\frac{R_c}{10^{10}}\right)^3 \left(\frac{N_W}{10^{10}}\right)^2 \left(\frac{\Delta \ell}{R_c}\right), \end{aligned} \quad (24)$$

where we assume a strong shock such that  $N = 4N_W$ , and  $R_c$  and  $N_W$  have both been scaled to the values used in the simulation. Using  $\Delta \ell = 0.1 R_c$ , the scale constant becomes  $EM_0 \approx 7 \times 10^{50} \text{ cm}^{-3}$ . As shown by WC07, typical EM values for line formation are  $\approx 10^{55} \text{ cm}^{-3}$ , implying that about  $10^4$  clumps would be required. Assuming simple Poisson statistics, the expected variability would then be about 1%, consistent with the low levels of X-ray variability from OB stars that has been previously noted. Interestingly, with  $EM_0 \propto R_c^3$  even small changes in the clump radius—certainly a poorly known quantity—have a significant impact on the predicted numbers of the clumps and expected levels of variability, suggesting that X-ray variability is a useful means of constraining clump properties (e.g., Oskinova et al. 2001).

Although the giants and MS stars with lower mass-loss rates (smaller optical depths) show more dispersion in the range of  $R_{\text{fir}}$ , there is no evidence of any X-ray emission arising from below the associated optical depth unity radii. Furthermore, regardless of luminosity class, none of the stars show high-energy ion stages forming far from the star. In the clump bow shock picture this means that the relative speed associated with the shocks is well below the ambient wind speed, which would produce very high temperatures. Clumps far from the star are likely being dragged out by the wind, and this reduces the shock temperatures in the outer regions, but with a sufficient shock jump in speed to produce the relatively low ion stages such as O VII and N VII.

As for the observed near-zero velocity shift and broad HWHM of the lines, these can best be explained if we have the X-ray line emission arising from the sides of the star as seen by the observer (i.e., perpendicular to the line of sight). This region contains a spread in speeds around the  $v_z = 0$  isovelocity surface. Such a concentration of emission from that sector of the wind would occur if there were “self-absorption” occurring. That is, each cool clump tends to absorb the line emission originating at the bow shock at the starward side of the clump. Thus, we see an enhanced contribution from the regions at, and symmetric about,  $v_z = 0$ . This counters the expected tendency to see the blueward-shifted and blueward-skewed line emission.

## 6. SUMMARY

One of the advantages of the clump bow shock picture is that it allows for a consideration of a three-dimensional model for the X-ray production from OB star winds. The bow shocks can be distributed randomly about the star or in some other prespecified way. Similarly, one could choose to assume a variety of clump sizes at any radial shell. So a variety of ideas can be tested with the bow shock picture. Accounting for bow shocks around clumps

in winds can potentially explain a number of properties of the X-ray emission observed from hot stars.

1. The wide range of ionization stages that occurs at essentially every radial distance from the star can be produced by bow shocks because of the power-law distribution of  $EM(T)$ . Low ion stages such as O VII occur far from the star, but not the highest ions. One might think that the shocks would be strongest there because the wind speed is the largest. However, clumps could be dragged out by the wind, and thus there could be a lower relative speed at large  $r$ , as discussed by Howk et al. (2000).

2. The zero centroid shift problem ( $V_{\text{peak}} \approx 0.0$ ) can be explained if the line radiation is generated primarily from clumps that are to the side of the star. This could occur because of the self-absorption effect, whereby the clumps along the line of sight to the star strongly attenuate the X-rays that are produced on the starward side of the clumps.

3. The broad line widths or HWHM of up to about half the wind speed can be caused by a combination of the sideways velocity of the bow shock flow plus a range in  $V_z$  values for an ensemble of clumps. This is in contrast with planar shocks that have been proposed for the shock fragments in hot star winds. The transverse velocity in the bow shocks is an essential aspect of the adiabatic or expansion cooling of the bow shock gas.

4. The narrower lines of main-sequence and giant stars can be explained by the correlation of wind speed with the transverse velocity around a clump. These stars have optically thin winds and the emission can be dominated by shocks located deeper in the wind, where the inflow speeds are slower.

5. The lines of high ion stages are not narrow as one might expect from source regions close to the star. However, to a large part this can be explained by the relatively low spectral (or velocity) resolution. For the *Chandra* HETGS/MEG spectra the HWHM resolution is about  $270 \text{ km s}^{-1}$  at  $25 \text{ \AA}$  for lines of low ion stages, and up to  $1300 \text{ km s}^{-1}$  for the high ions. The transverse velocity behind a clump and the range in clump velocities would lead to further broadening.

6. There are observed  $EM(T)$  power laws (e.g., WS05), and these result directly from the wind-oblique shock interactions.

The shape of the  $EM(T)$  distribution depends on the fraction of the wind material lying above optical depth unity.

7. The  $R_{\text{fir}}$  radius corresponds rather well to the radius of optical depth unity, and this can probably be explained by having the observed line formation sources located to the sides of the star relative to the line of sight to the observer and having the mass-loss rate reduced by an acceptable amount, such as  $1/3$  the traditional  $\dot{M}$  values.

In addition to a consideration of the problems summarized above, we have introduced the OTSh picture. This provides a way to derive the line source information and the line-of-sight Doppler velocity shifts needed to compute line profiles from a single clump or an ensemble of clumps distributed through a wind.

The clump bow shock picture forms a useful element in a more realistic 3D view of the stellar winds of hot stars, and the OTSh approach forms a useful technique for predicting and analyzing X-ray emission properties. The results should be of interest in areas other than hot star astronomy. Clump flow interactions are thought to occur in objects such as RS Oph (Nelson et al. 2008). Clumps with bow shock interfaces with a wind are seen in *Hubble Space Telescope* images of planetary nebulae (O'Dell & Handron 1996). An understanding of clumps can also affect research well beyond the stellar wind community.

We thank Nick Moeckel for early work on the  $EM(T)$  relation and Greg Tracy for producing some of the figures. We are also grateful to John Brown for many interesting conversations on the topic of wind clumps. J. P. C., R. I., A. L., and N. A. M. have been supported in part by award TM3-4001 issued by the *Chandra* X-ray Observatory Center. We also acknowledge support from the NSF Center for Magnetic Self Organization in Laboratory and Astrophysical Plasmas. W. L. W. acknowledges support by award GO2-3027A issued by the *Chandra* X-ray Observatory Center. *Chandra* is operated by the Smithsonian Astrophysical Observatory under NASA contract NAS8-03060.

#### REFERENCES

- Abbott, D. C., Biegging, J. H., & Churchwell, E. 1981, *ApJ*, 250, 645  
 Barlow, M. J., & Cohen, M. 1977, *ApJ*, 213, 737  
 Bouret, J.-C., Lanz, T., & Hillier, D. J. 2005, *A&A*, 438, 301  
 Bouret, J.-C., et al. 2003, *ApJ*, 595, 1182  
 Brown, J. C., Ignace, R., & Cassinelli, J. P. 2000, *A&A*, 356, 619  
 Brown, J. C., Telfer, D., Li, Q., Hanuschik, R., Cassinelli, J. P., & Kholtygin, A. 2004, *MNRAS*, 352, 1061  
 Burke, A., Ignace, R., & Cassinelli, J. P. 2006, *BAAS*, 38, 1046  
 Canto, J., & Raga, A. 1998, *MNRAS*, 297, 383  
 Cassinelli, J. P., & Abbott, D. C. 1981, in *The Universe at UV Wavelengths*, ed. R. D. Chapman (Washington: NASA), 127  
 Cassinelli, J. P., Brown, J. C., Maheswaran, M., Miller, N. A., & Telfer, D. C. 2002, *ApJ*, 578, 951  
 Cassinelli, J. P., Castor, J. I., & Lamers, H. J. G. L. M. 1978, *PASP*, 90, 496  
 Cassinelli, J. P., & Hartmann, L. 1977, *ApJ*, 212, 488  
 Cassinelli, J. P., & Olson, G. L. 1979, *ApJ*, 229, 304  
 Cassinelli, J. P., & Swank, J. H. 1983, *ApJ*, 271, 681  
 Cassinelli, J. P., et al. 1995, *ApJ*, 438, 932  
 ———. 1996, *ApJ*, 460, 949  
 Cho, J., & Lazarian, A. 2002, *Phys. Rev. Lett.*, 88, 245001  
 Cohen, D. H., Leutenegger, M. A., Grizzard, K. T., Reed, C. L., Kramer, R. H., & Owocki, S. P. 2006, *MNRAS*, 368, 1905  
 Cooper, R. G. 1994, Ph.D. thesis, Univ. Delaware  
 Cox, A. N., ed. 2000, *Allen's Astrophysical Quantities* (4th ed.; Berlin: Springer)  
 Donati, J.-F., Babel, J., Harries, T. J., Howarth, I. D., Petit, P., & Semel, M. 2002, *MNRAS*, 333, 55  
 Donati, J.-F., et al. 2006, *MNRAS*, 370, 629  
 Eisloffel, J., Mundt, R., & Bohm, K. H. 1994, *AJ*, 108, 1042  
 Evans, C. J., Crowther, P. A., Fullerton, A. W., & Hillier, D. J. 2004, *ApJ*, 610, 1021  
 Feldmeier, A., Oskinova, L., & Hamann, W.-R. 2003, *A&A*, 403, 217  
 Feldmeier, A., Puls, J., & Pauldrach, A. W. A. 1997, *A&A*, 322, 878  
 Fullerton, A. W., Massa, D. L., & Prinja, R. K. 2006, *ApJ*, 637, 1025  
 Hamann, W.-R., Feldmeier, A., & Oskinova, L. M., eds. 2007, *Proc. International Workshop on Clumping in Hot-Star Winds* (Potsdam: Potsdam Univ.)  
 Harnden, F. R., Jr., et al. 1979, *ApJ*, 234, L51  
 Hayes, W. D., & Probstein, R. F. 1966, *Hypersonic Flow Theory*, Vol. 1, (New York: Academic Press)  
 Hillier, D. J. 1991, *A&A*, 247, 455  
 Hirschi, R. 2007, in *Proc. International Workshop on Clumping in Hot-Star Winds*, ed. W. R. Hamann, A., Feldmeier & L. M. Oskinova (Potsdam: Potsdam Univ.), 9  
 Howk, J. C., Cassinelli, J. P., Bjorkman, J. E., & Lamers, H. J. G. L. M. 2000, *ApJ*, 534, 348  
 Ignace, R., & Gayley, K. 2002, *ApJ*, 568, 954  
 Lamers, H. J. G. L. M., & Morton, D. C. 1976, *ApJS*, 32, 715  
 Lamers, H. J. G. L. M., & Rogerson, J. 1978, *A&A*, 66, 417  
 Lepine, S., & Moffat, A. 1999, *ApJ*, 514, 909  
 Leutenegger, M. A., Paerels, F. B. S., Kahn, S. M., & Cohen, D. H. 2006, *ApJ*, 650, 1096  
 Li, Q., Cassinelli, J. P., Brown, J. C., Waldron, W. A., & Miller, N. A. 2008, *ApJ*, 672, 1174  
 Liu, X., & Osher, S. 1998, *J. Comput. Phys.*, 141, 561  
 Lomax, H., & Inouye, M. 1964, *NASA Tech. Rep. R-204* (Washington: NASA)

- Lucy, L. B. 1982, *ApJ*, 255, 286
- Lucy, L. B., & Solomon, P. M. 1970, *ApJ*, 159, 879
- Lucy, L. B., & White, R. L. 1980, *ApJ*, 241, 300
- Lupie, O. L., & Nordsieck, K. H. 1987, *AJ*, 93, 214
- MacFarlane, J. J., & Cassinelli, J. P. 1989, *ApJ*, 347, 1090
- MacFarlane, J. J., Cassinelli, J. P., Welsh, B. Y., Vedder, P. W., Vallerger, J. V., & Waldron, W. L. 1991, *ApJ*, 380, 564
- Massa, D., Fullerton, A. W., Sonneborn, G., & Hutchings, J. B. 2003, *ApJ*, 586, 996
- Miller, N. A., Cassinelli, J. P., Waldron, W. L., MacFarlane, J. J., & Cohen, D. H. 2002, *ApJ*, 577, 951
- Moeckel, N., Cho, J., & Cassinelli, J. P. 2002, *BAAS*, 34, 772
- Nelson, T., Orio, M., Cassinelli, J. P., Still, M., Liebowitz, E., & Mucciarelli, P. 2008, *ApJ*, 673, 1067
- Nugis, T., & Lamers, H. J. G. L. M. 2000, *A&A*, 360, 227
- Odegard, N., & Cassinelli, J. P. 1982, *ApJ*, 256, 568
- O'Dell, C. R., & Handron, K. D. 1996, *AJ*, 111, 1630
- Oskinova, L. M., Feldmeier, A., & Hamann, W.-R. 2004, *A&A*, 422, 675
- . 2006, *MNRAS*, 372, 313
- Oskinova, L. M., Ignace, R., Brown, J. C., & Cassinelli, J. P. 2001, *A&A*, 373, 1009
- Owocki, S. P., Castor, J. I., & Rybicki, G. B. 1988, *ApJ*, 335, 914
- Owocki, S. P., & Cohen, D. H. 2006, *ApJ*, 648, 565
- Seward, F. D., Forman, W. R., Giacconi, R., Griffiths, R. E., Harnden, F. R., Jr., Jones, C., & Pye, J. P. 1979, *ApJ*, 234, L55
- Smith, R. K., Brickhouse, N. S., Liedahl, D. A., & Raymond, J. C. 2001, *ApJ*, 556, L91
- Waldron, W. L., & Cassinelli, J. P. 2001, *ApJ*, 548, L45
- . 2007, *ApJ*, 668, 456 (WC07)
- Wojdowski, P., & Schulz, J. P. 2004, *ApJ*, 616, 630 (WS04)
- . 2005, *ApJ*, 627, 953 (WS05)